# Structural Modeling for the Terrestrial Planet Finder Mission

Andrew Kissil[*a], Eug Kwack[a], Timothy Ho[a], Alice Liu[b], Carl Blaurock[c]
[a]Jet Propulsion Laboratory, 4800 Oak Grove Drive, Pasadena, CA, USA 91109-8099
[b]Goddard Space Flight Center, Greenbelt, MD, USA 20771
[c]Mide Technology Corporation, 200 Boston Ave, Suite 1000, Medford, MA, USA 02155

## ABSTRACT

The Coronagraph version of the Terrestrial Planet Finder (TPF) mission relies on a large-optics, space-born observatory, which requires extreme stability of the optics in the presence of thermal and dynamic disturbances. The structural design requires balancing of stringent constraints on launch packaging with unusually tight response requirements for thermal and dynamic environments.

The minimum-mission structural model (pre-phase A, point design) includes a deployable, pre-tensioned membrane, sun-shield and solar-sail, a 10m long deployable secondary support structure, and a light-weighted 6m diameter monolithic glass primary mirror. We performed thermal distortion and dynamic response analyses in order to demonstrate feasibility, quantify critical sensitivities, and to identify potential problems that might need to be addressed early on.

**Keywords:** coronagraph, planet finder, telescope, deployable, sun-shield, large-optics

## 1. INTRODUCTION

The Terrestrial Planet Finder (TPF) mission, as part of the NASA Origins Program, is tasked with finding and characterizing, over a period of 5 years, earth-like planets in near-by star systems that may provide environments suitable for sustaining life. Currently, we are considering the launch of both coronagraph and interferometer-based space-born observatories, which complement each other as to star target lists and science capabilities. This paper describes a point-design, for a "pre-phase A" concept of a coronagraph-based system, and represents a possible design approach, which is aimed at satisfying minimum science requirements: i.e. surveying 35 stars, and searching habitable zones to 95 percent completeness in the visible spectral range. This design represents a snapshot in time of the design evolution process, and as such, we are also looking at other designs that may be capable of surveying more stars, but these other designs will not be addressed in this paper.

Two environmental disturbance sources were identified as being critical to the system design, and were therefore addressed first in our analytical approach. One critical environmental disturbance occurs during the planet detection phase. The design team decided to pursue the use of telescope dithering: the rotation of the telescope about the line-of-sight (LOS) by approximately 20 degrees, without adjustment or compensation with the deformable mirror or any element alignment actuation. Ideally, during the dithering maneuver, the speckles should remain stationary in the target image, and the planet image should move with respect to the speckles. There are other promising methods for speckle removal, not requiring the dither maneuver that are being pursued as well, but they are not considered to be mature enough at this time to be adopted in our baseline approach. Since the deformable mirror cannot be adjusted during the dithering phase, the system must be very thermally stable, even while Sun exposure is changing on the outer sun-shield surface.

Another critical environmental disturbance source is the vibration induced by the normal operation of the reaction wheels, used in the pointing control system. The reaction wheels are used for pointing control in target acquisition, and for stabilization during observation. Since reaction wheels can never be perfectly manufactured, static and dynamic wheel imbalances, as well as bearing imperfections, induce forces and torques that propagate through the system and

can effect optical alignment and optical element distortion, causing image aberration. In order to model this disturbance propagation, the dynamic model must have enough fidelity to capture the system response to this type of disturbance.

### 1.1. Orbit and Launch Vehicle Selection

The current orbit baseline is a heliocentric, 1AU, earth drift-away orbit, similar to that selected for the Spitzer Telescope (formerly SIRTF). The earth separation rate would be about 0.1 AU per year. This orbit provides a very stable thermal environment, with a near constant solar flux, and there are no propulsive delta-V's required[1]. The Delta IV-Heavy, Boeing launch vehicle was selected for our baseline design. With this vehicle, we have a lift capacity of about 10,000 kg (not including margin) to $C_3$ of 0.4. The launch payload fairing is about 5m in diameter, and has a 13m long straight section (19m to fairing nose)[2].

### 1.2. System Description

The TPF minimum mission flight system configuration has the following major components: a science payload, consisting of a telescope and instrument; a spacecraft bus with a v-groove type sun-shield, solar sail and solar array; and a launch support structure. Figure 1 shows a plot of the deployed observatory, with dimensions indicated: the overall length is about 37 m (121 ft). The dedicated launch support structure is ejected after completion of the launch phase.

The telescope, comprised of the primary and secondary mirrors and intermediate support structure, is an off-axis Cassegrain-type design, with a 10 m separation between the primary and secondary mirrors. The primary mirror is a monolithic light-weighted (front & back face-sheets with honeycomb core) 6 m by 3.5 m elliptical glass mirror (0.25 m overall thickness), made from Ultra-Low Expansion (ULE™) glass, and the secondary mirror is another light-weighted ULE™ mirror, 0.7 m by 0.44 m. The combination produces a F/20 beam, with F-number considered along the major axis. The secondary mirror is mounted on the end of a deployable tower, constructed of M55J/954-3 carbon fiber reinforced polymer (CFRP) composite material, having three folding (hinged & latched) joints. Figure 2 shows a cut-away of the v-groove sun-shield, revealing the deployed telescope.

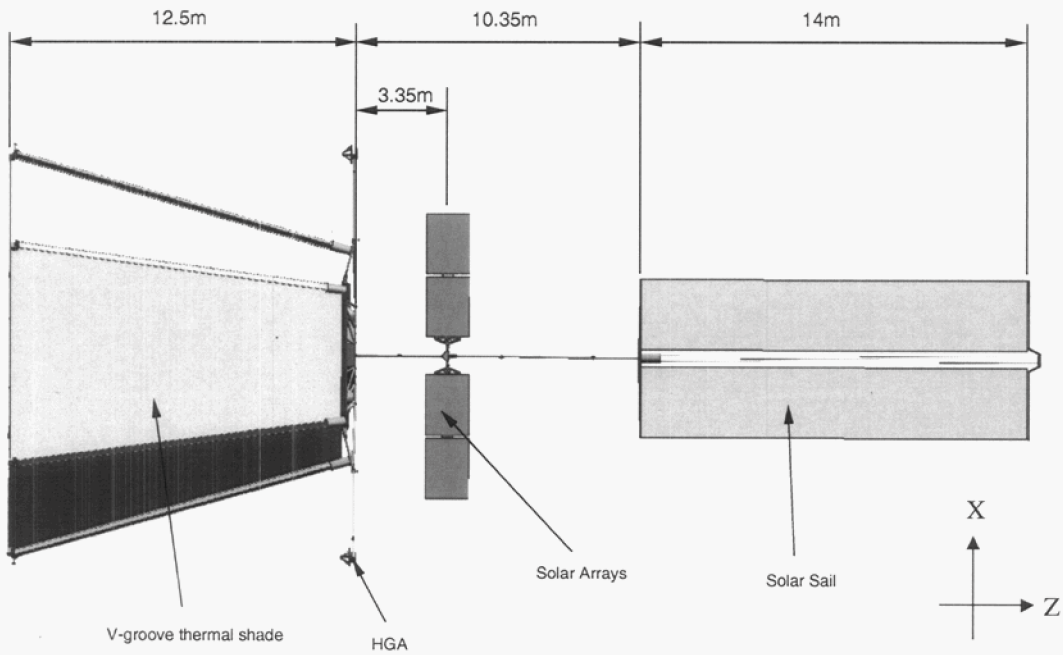


Fig. 1.2.1. Fully Deployed Observatory

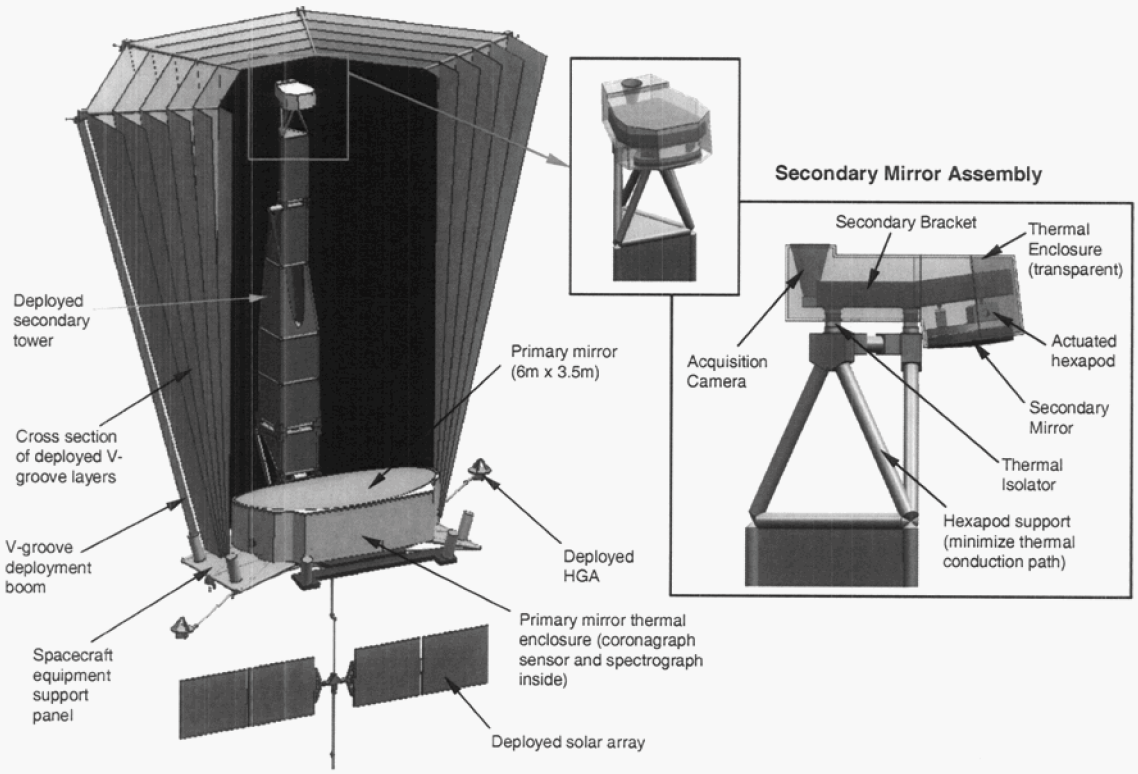


Fig. 1.2.2. Telescope with Secondary Mirror Assembly Detail.

The primary mirror, it's support structure and instrument box are housed in a thermal enclosure, which will maintain a relatively constant temperature, near room temperature. The secondary mirror is also housed in its own thermal enclosure, while the support tower temperature is allowed to passively reach equilibrium, without active control.

The baseline system design allows for limited active motion compensation, using the secondary mirror, a fast steering mirror, and a deformable mirror. The secondary mirror rigid-body motion can be controlled with feedback provided by a metrology system, for response to frequencies less than approximately 1 Hz. The secondary mirror is mounted on a hexapod-type actuator, which can control all six rigid-body degrees of freedom. This will allow compensation for tower distortions due to changes in thermal environment after slew maneuvers. Higher frequency responses, such as responses to reaction wheel disturbance, cannot be compensated by the secondary mirror hexapod system, without a great deal of design effort and expense. The fast steering mirror is used in the pointing control system, and the deformable mirror is used to compensate for primary mirror distortions.

The telescope assembly is mounted to the spacecraft bus, using a vibration isolation system. Although we expect that ultimately an active isolation system would be needed, or first analytical approach was to assume a passive isolation system, to quantify the necessity for the more costly and complex active isolation. Figure 3 shows a schematic diagram of the deployed system, showing the location of the dynamic isolators. Our first assumption was that we would have a 1 Hz isolator between the telescope and spacecraft bus. However, reaction wheel jitter analysis, using Goodrich/TW-50E300 type wheels, showed us that a second stage of isolation, with a frequency of 2 Hz, was needed at the reaction wheel assembly attachment, and that the telescope/spacecraft isolation frequency needed to be reduced to 0.75 Hz in order to meet requirements.

A "cocoon" type of sun-shield, using 6 v-groove layers, is used for this baseline design. A flat sun-shield is also being looked at, but such a system introduces a new set of complications, such as gimbaling. The v-groove radiator consists of 6 layers of shielding of ~0.05 mm thick Kapton™. Each side of the Kapton™ is coated with ~ 1000 angstroms of vapor-deposited aluminum (VDA) to reduce radiant coupling between shield layers. This material is highly specular at

the relatively long IR wavelengths associated with the internal shield layers. The two exceptions to this are the inner and outermost surfaces. The inner surface is optically black in order to provide stray light control around the primary and secondary mirrors.

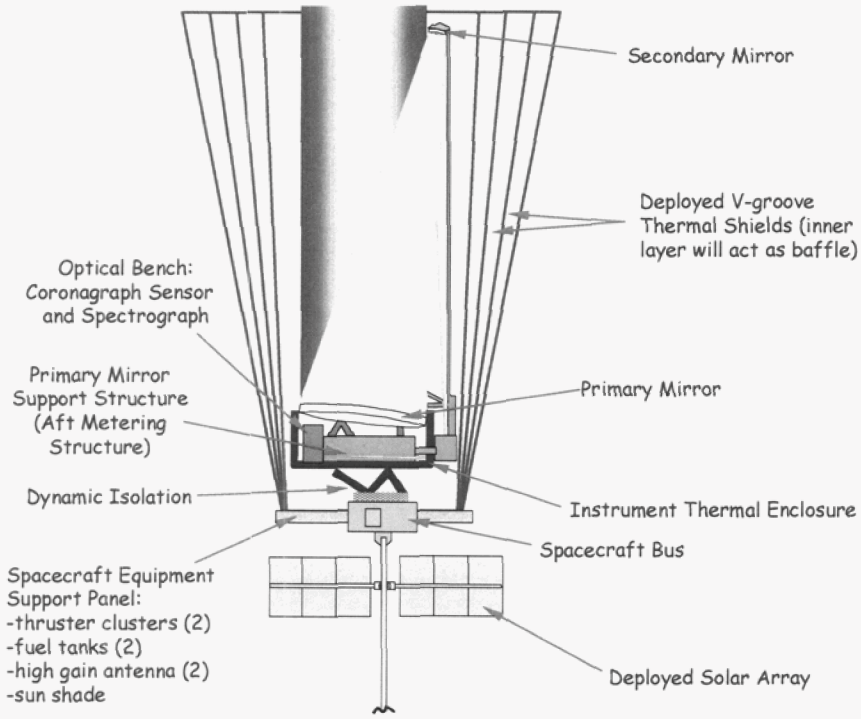


Fig. 1.2.3. Configuration Schematic.

### 1.3. Scope of Modeling and Analysis

The main goal for the analytical modeling the minimum mission configuration is to demonstrate feasibility, at least on paper, quantify critical sensitivities, and to identify potential problems that might need to be addressed early on. It will be shown that system responses to the expected thermal and dynamic disturbances show satisfactory performance with respect to the requirements budget, which is traceable to estimated contributions to planet/star contrast. By satisfactory performance, we mean that no "show-stoppers" have been identified that cannot be addressed with good engineering practice. Clearly, we are just scratching the surface of a very complex system design, and many details need to be completed in future work.

A structural finite element model (FEM) was generated for the stated purposes of preliminary design feasibility studies. The model size was intentionally kept small enough to allow rapid re-processing for trade studies, and was made detailed enough to capture the first order structural effects, within an expected accuracy of generally 10 to 20%. The system structural model is applicable for linear static and dynamic analysis, using small displacement theory. No attempt was made, as yet, to model the non-linearity of the hinges and latches at this time. The effects of hinge and latch non-linearity will be addressed separately in future studies and test-beds.

Linear material properties were assumed, including coefficients of thermal expansion. It was assumed that the nominal tangent cte's could be used without integrating over a temperature range. This assumption is valid if the cte's don't change significantly over the temperature range encountered in the analysis. Conservative, bounding values for cte's were generally used for all materials. The effect of cte variation, with respect to spacial distribution, for mirror substrate material (ULE™) is investigated in some depth, and the results are described in this paper.

The analyses presented in this paper include thermal distortion analyses, and dynamic characterization (normal modes) analyses. Thermal distortion analyses were performed for the dither maneuver, a 20 degree roll about the LOS: both steady-state and transient thermal analyses were conducted. The normal modes analysis provides insight into the system dynamic characteristics, and provides results that are used in reaction wheel jitter and attitude control analyses. The reaction wheel jitter analyses involved computing the frequency response of the LOS and wave-front error (WFE) to the expected disturbance caused by the normal operation of reaction wheels.

## 2. MODEL DESCRIPTION

### 2.1. Overall Model

Three different models were used for analyzing the system response: a low-fidelity, a mid-fidelity, and a high-fidelity model, with model sizes ranging from 17,000 to 110,000 degrees of freedom. The difference between the three models was in the detail of the primary mirror component model. The low-fidelity primary mirror model consisted of a single layer of 2D plate elements with effective bending & shear, matching overall mirror mass and stiffness properties, but neglecting through thickness compliance, and print-through effects. The three models compared very well with respect to dynamic characteristics. The total model mass for the deployed minimum mission FEM was approximately 5,400 kg, not including launch support structure.

### 2.2. Primary Mirror Model

The primary mirror, considered the most critical component of the system, was modeled using the highest level of detail present in the system model. The primary mirror construction is integrally linked with the composition of the FEM, since constituent properties variations need to be addressed. Similarly, the analysis rigor was biased toward capturing the primary mirror response. The baseline primary mirror design has a light-weighted honeycomb sandwich type of construction, with two face-sheets separated by a honeycomb core. Our design assumes that the mirror will be constructed by joining 21 segments together, as shown in Fig. 2.2.1, using a predominantly hexagonal shape for the individual segments. The final joining, or fusing, process results in a monolithic glass mirror.

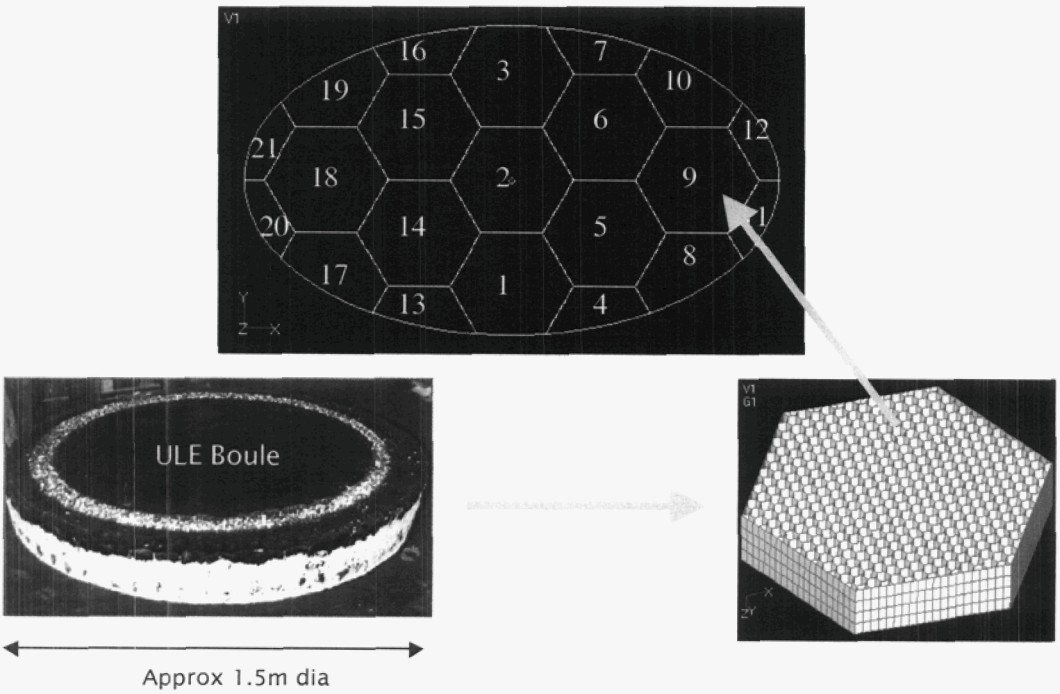


Fig. 2.2.1. ULE™ Boule, Single Segment Core and Segment Layout for Primary Mirror

The basic mirror segment is hexagonal, measuring 1.2 m flat-to-flat, based on what can be accommodated with ULE™ boules, which are approximately 1.5 m in diameter. However, there are six segments that are only partial hexagons, in order to accommodate the overall elliptical shape of the primary mirror. Each of the segments also has an edge wall around its perimeter. The segments are located adjacent to each other, but are only structurally connected via the face-sheets. In other words, there is a small gap between the edge walls of adjacent segments.

The overall mirror design parameters are as follows: length = 6 m, width = 3.5 m, thickness = 0.25 m. The internal design parameters are the following: front face-sheet thickness = 6 mm, back face-sheet thickness = 3 mm, honeycomb core wall thickness = 1.4 mm, core edge thickness = 1.4 mm. Since standard ULE™ boules are approximately 6 inches (0.152m) thick, we would need to stack and fuse two boules together, in order to construct each core segment.

### 2.3. Modeling Of Tensioned Membranes

The sun-shield and solar-sail use pre-tensioned membranes to provide adequate stiffness. The stiffening effect of the pre-tensioned membrane is incorporated directly into the model, using effective element properties. In particular, it was important to adequately capture the low frequency modes that might influence the attitude control system, as well as modes that might couple with the dynamics of the critical optical elements of the telescope. The conventional approach to modeling pre-tensioned members is to require two analysis runs: a preliminary preload application to generate the differential stiffness matrix, and then the application of external loads. The approach chosen here for modeling the pre-tensioned membranes incorporates a novel approximation of the geometric or load-stiffening effects, using the equivalent shear stiffness of standard plate elements. A similar approach can be used for modeling load-stiffened cables, or load-softened beams, using the standard beam element shear stiffness. Using the shear stiffness allows the sequence of modal frequencies to increase proportional to "i" (mode number), rather than "$i^2$" as one would get using the bending stiffness, the former being the case for load-stiffened cables and membranes as well. If one uses the bending stiffness to approximate the geometric stiffness, then only the first mode frequency can be matched: the higher modes would increase in frequency at a much higher rate, with respect to mode number, than would be the case associated with using the correct geometric stiffness.

Another positive feature of using the standard element (beam or plate) shear stiffness to represent the geometric stiffness of load-stiffened structures is that there is no artificial grounding of the stiffness matrix, as one encounters with many geometric stiffness formulations used in commercial FEM programs. Artificial grounding is especially detrimental for free-free systems, as we have with a space-born telescope.

The modeling process for the load-stiffened members is simplified somewhat if one can make the assumption that bending stiffness is very minor compared the load-stiffening effects. If the stiffness is dominated by the load-stiffening effects, one can remove the bending stiffness from the problem by assigning an artificially high bending stiffness, such that the associated bending modes would occur at high enough frequencies that they are above the frequency range of interest. However, the bending stiffness should not be so high as to cause ill-conditioning problems. If bending stiffness is an important factor, then a parallel set of nodes and elements can be defined on top of the elements used for modeling load-stiffening, and only the translational degrees of freedom would be connected between the two node sets.

Another caveat is in the assumption of uniform preload stress. In reality, the preload stress will vary over the membrane, and may even go to zero in certain regions, allowing wrinkling and/or flapping. The modeling approach described herein doesn't account for such occurrences, but is mainly aimed at providing an early-on design aid, describing an ideal system. Once a feasible design is obtained, further detailed design and analysis should be persued to address these issues, and how they might effect performance.

To model the load-stiffened membrane, the plate thickness and material properties are defined as usual. The bending factor should be set to a high value (again, not too high) to remove the bending flexibility from the model low frequency characteristics. The shear stiffness can then be tuned to match the correct geometric stiffness due to preload. The shear stiffness factor (TS/T in the NASTRAN PSHELL element property definition) should be set to the following:

Shear Factor = Preload/G

where the Preload is the biaxial tension stress (i.e. $lbs/in^2$ or $N/m^2$, etc), and G is the material shear modulus. For our v-groove model, we used 20703 Pa (3 psi) for preload tension, and a G value of 1.312 GPa (190 ksi) for the Kapton™ membrane material. The in-plane membrane characteristics are not adversely affected by the above modeling definitions. The parameters used in the NASTRAN mode are as follows: the shear factor (TS/T) = 1.578E-5 = 20703/1.312E+9, and bending factor (12I/T^3 ) = 1e+9.

## 3. ANALYSIS DESCRIPTION

### 3.1. Thermal Distortion Analysis

As mentioned above, thermal stability during a "dithering" maneuver was considered a critical performance characteristic for our system. Because of the elliptical shape of our primary mirror, we required two dither maneuvers to be performed at clocking angles 90 degrees apart. Each of the dither maneuvers involves making two observations, 20 degrees apart. Figure 3.1.1 shows a view looking from the target star toward the observatory, with the Sun angles indicated for one dither maneuver. It turns out that the other dither clocking position, 170 to 180 degree azimuth, was found to be less severe thermally than the 80 to 100 degree case. Also, as a worst-case scenario, the Sun was positioned such that the direction of travel of the Sunlight was orthogonal to the bore-sight direction. This gives the maximum energy impingement on the sunshield. Normally, the Sun's position is restricted to be anywhere in the hemisphere side which is opposite to the viewing side of the telescope, such that Sunlight is prevented from entering the v-groove openings.

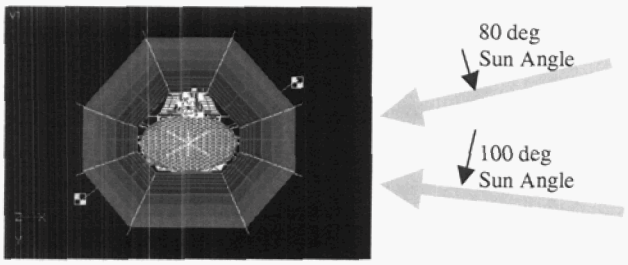


Fig. 3.1.1 View of the Sun Angles for the Worst-Case 20 degree Dither Maneuver

In order to quantify the system stability, we started with a series of thermal analyses: computing the steady state and transient temperature changes to be expected. These temperature changes were then applied as boundary conditions for our system FEM, in order to compute the resulting distortions. Although the distortion of the secondary support tower is considered an important factor contributing to system performance, as long as it is within the compensatable range of the secondary actuation, it is not as critical as the primary mirror distortion.

As part of the thermal distortion analysis, we studied the effects of variation of coefficient of thermal expansion (CTE) on system performance. We wanted to quantify the sensitivity of primary mirror distortion to material CTE spacial variability. For most of our preliminary thermal distortion analyses, we assumed a nominal CTE value of 30 ppb/C. Since the ULE™ glass manufacturer specifies that the CTE for optical grade glass can vary anywhere between –30 ppb/C and +30 ppb/C, we needed to investigate the potential implications for possible CTE variations.

Our first step was to adopt a somewhat more stringent set of CTE material specifications than would be expected for general off-the-shelf ULE boules, yet realizable within current manufacturing practices. Table 3.1.1 presents the set of CTE tolerance specifications imposed on the Technology Development Mirror (TDM). This set of tolerances will be adhered to, until we determine whether more stringent ones might be required, or whether they can be relaxed.

Table 3.1.1 Material CTE Specifications Used for the TDM

| INITIAL MIRROR CTE TOLERANCES | | |
|---|---|---|
| No. | Description | Tolerance (ppb/C) |
| 1 | Weighted Blank Average | +/- 10 |
| 2 | Core Segment Axial Gradient | +/- 10 |
| 3 | Core Segment Radial Range | < 15 |
| 4 | Max Core Segment-Segment Average Delta | < 10 |
| 5 | Face Plate Axial Gradient | +/- 5 |
| 6 | Face Plates Pt-to-Pt Difference | < 5 |
| 7 | (Face Plate Average) - (Core Segment Average) | +5 to +15 |

The question of how to vary the material CTE within the structure of the primary mirror is also a very important issue. If we were to allow the CTEs to vary randomly throughout the structure at microscopic levels, the effect would be less harmful to performance than considering variations between macroscopic regions. The variation between regions is also more realistic, since certain segments of the mirror are manufactured separately, using different boules of glass, and then joined in a later process. The CTE variations within glass boules have been studied to some degree, and have been characterized. For instance, we know from typical boule measurements that the CTE may vary radially, but is fairly constant azimuthally (to measurement precision). However, the orientation of the original boule within the final mirror-blank assembly may vary with how the constituent piece was machined.

In our studies, the CTE was varied by region. There are 84 basic regions in the primary mirror model, originating from different glass boules: 4 layers x 21 segments. The 4 "layers" are comprised of the two face sheets plus two core components. Functions were used for representing CTE variations within the 84 regions, and are described by the following: bias or piston variation, side-to-side variation along x & y-direction, radial variation (in x-y plane), and axial variation (along the z-dir, which is used for core segments only).

A standard "Monte-Carlo" approach was used, in which 1000 random trials represented possible CTE variations within the primary mirror FEM. The CTEs were varied in a manor consistent with the CTE specifications for the TDM (see Table 3.1.1), via the uniform random variation of function parameters described above.

The final phase of the study included a simplified optimization of glass boule placement, based on minimization of wave-front error (WFE). The WFE is a good metric for minimization, since it can be related to system contrast. The idea is that the glass CTEs can be measured fairly accurately prior to the final mirror blank assembly operation. If we know what our worst-case temperature disturbance is, we can place the glass segments in optimal positions prior to the final fusion process. Similar approaches of optimal glass placement have been used successfully for the construction of the SUBARU and GEMINI mirrors. For our study, we took the mirror segment CTE values for the worst-case sample (of the 1000), based on overall WFE, and then located the near-best placement for the segments, resulting in minimizing the WFE.

### 3.2. Normal Modes Analysis

The normal modes (dynamic vibration) analyses were performed using NASTRAN. We looked at cantilevered modes of component structures, as well as the free-free modes of the system. The free-free system modes were eventually used for attitude control performance analysis, as well as for disturbance jitter evaluation during observation.

### 3.3. Reaction Wheel Jitter Analysis

The LOS jitter and dynamic WFE analyses are performed on the open loop structural model, for the following reasons. The ACS loop can be ignored since its bandwidth is below the lowest reaction wheel assembly (RWA) disturbance, and therefore it does not influence the response to RWA disturbance. The FSM control loop is limited to roughly 10Hz bandwidth. The plant response shows exceedances at well above this frequency, so that the system design cannot rely on the FSM to compensate for dynamic jitter.

The first-cut analysis was performed on the baseline structural model, using Goodrich (Ithaco) E wheels, with one stage of isolation at 1Hz between the bus and the Aft Metering Structure (AMS isolation), with the RWA assembly hard-mounted to the bus. This was shown to be inadequate: a second isolation stage was added at the RWA attachment (2 Hz), and the bus/AMS isolation frequency was reduced to 0.75 Hz. The nominal structural damping was 0.5%, with 5% damping applied to the isolator using physical damping elements. The RWAs were oriented with 3 wheels in orthogonal directions and the 4$^{th}$ wheel at 45 degrees to all axes.

# 4. ANALYSIS RESULTS

## 4.1. Thermal Distortion Analysis Results

The system temperature changes were computed for the worst-case "dither" maneuver described above, in which the angle of incident Sunlight was changed by 20 degrees clocking angle (see Fig. 3.1.1). The primary mirror FEM nodal point transient temperature changes are plotted in Fig. 4.1.1. These are the temperature changes that occur over a 24 hour period, after the observatory is rotated 20 degrees about the bore-sight axis. We see a peak-valley temperature change of approximately 0.5 mK over the 24 hour period. Figure 4.1.2 shows the transient response of the change in average back to front temperature difference, which can be correlated to driving a change in mirror focus.

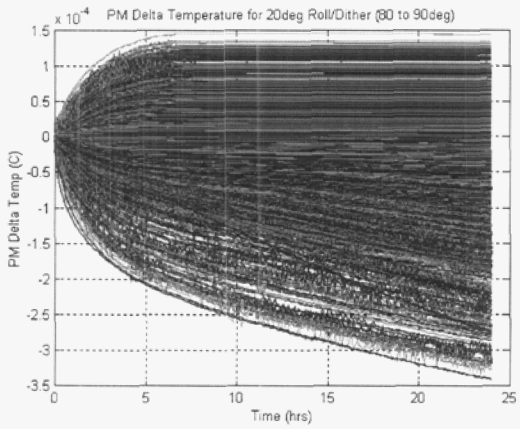


Fig. 4.4.1. Primary Mirror Transient Temperature Changes

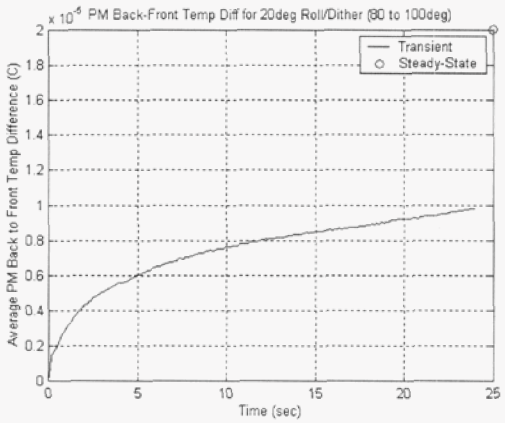


Fig. 4.4.2 Change in Average Back to Front Temperature Difference

Fig. 4.4.3 shows a summary of WFE response (m, rms) to primary mirror distortion, due to steady-state temperature changes caused by the worst-case dither maneuver. Stead-state is a worst-case scenario, since the actual observation time needed after the dither would be on the order of a few hours. The x-axis indicates the Zernike component of the WFE, and the y-axis indicates the response magnitude, with range of 0 to 6 picometers. Small circles show the requirement specifications, derived from a contrast budget. The triangles show the response for the case of using a uniform glass CTE of 30 ppb/C. The points indicated by plus markers, connected with a dotted line, represents the 3-sigma response for the case of varying CTEs as described in section 3.1. The solitary dots show the response for the worst-case (based on total WFE) sample, selected from the 1000 samples used in the Monte-Carlo analysis. The solitary plus markers, without dotted lines, indicate the response obtained for the case of optimal segment placement.

We see that the response for the uniform 30 ppm/C case exceeds the Monte-Carlo study results for the focus term (Zernike 4), but under-predicts the response for the higher order Zernikes. The Monte-Carlo study results, without segment placement optimization, exceed the requirements for all Zernike components. Using the optimal segment placement, however, allows us to meet the requirement specifications, with coma being the worst-case, i.e. smallest margin.

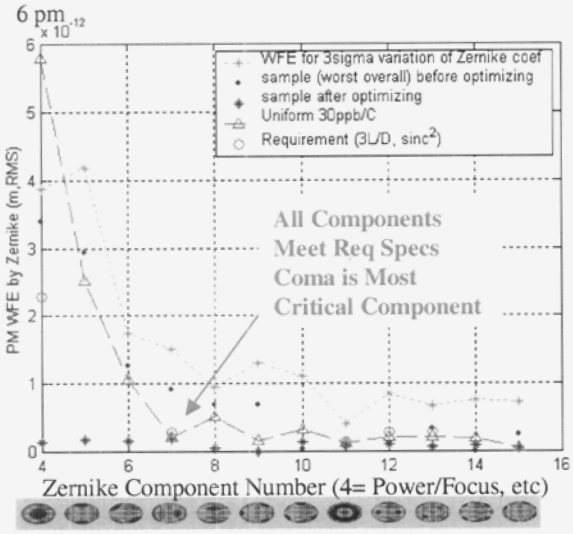


| | 80 to 100 deg Dither | | |
|---|---|---|---|
| Zernike Comp | Stead-State Resp (pm) | 3L/D Req Specs (pm) | Ratio Req/Resp |
| 4 | 0.14 | 2.29 | 16.21 |
| 7 | 0.19 | 0.29 | 1.47 |
| 11 | 0.09 | 0.14 | 1.64 |
| 12 | 0.11 | 0.29 | 2.53 |
| 13 | 0.07 | 0.29 | 3.86 |

Fig. 4.4.3. Primary Mirror Zernike Response for Steady-State Temperature Changes due to a Dither

### 4.2. Normal Modes Analysis Results

For most of the dynamic analyses conducted with our structural model we were concerned with responses out to about 100Hz. For this reason we generally keep structural vibration modes out to 3x the maximum frequency of interest, or 300Hz in this case. For the combined system model there are 1386 modes out to 300 Hz. For the Payload model there are 115 modes out to 300 Hz, and for the Support Module model there are 1271 modes out to 300 Hz. The first secondary tower-bending mode was found to be at about 13 Hz, and a coupled torsion-lateral bending mode was at 16 Hz. The first primary mirror-bending mode occurs at about 40 Hz.

Figure 4.2.1 shows a plot of the frequencies for the combined system model vs. mode number for the first 1400 modes, out to about 300 Hz. We can see from the plot that there are many low frequency modes: there are over 250 modes below 5 Hz. Most of these low frequency modes are due to the presence of the sun-shield and solar array components.

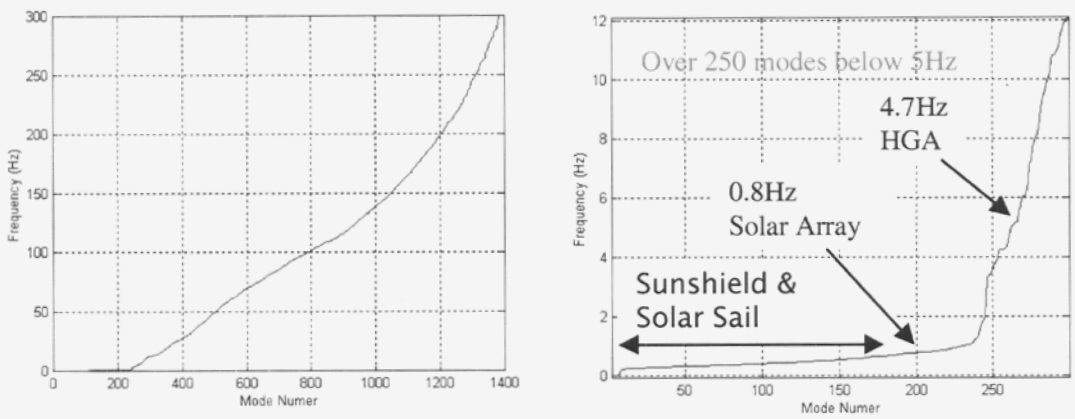


Fig. 4.2.1. Full System Model Normal Mode Frequencies

The minimum sun-shield frequency was expected to occur at the outer (forward) edge of the widest flat segment (7.372 m wide). The shape of this flat segment of the V-groove is approximately trapezoidal, with two equal length segments 12.5 m long, a 7.372 m long side, and a 4.4 m long side. Two hand calculations were performed, using Ref. 3, to

estimate the expected first mode frequency: one with a fixed boundary rectangle 24 m (twice the height of the trapezoid) by 7.372 m, and one with a 12m by 7.372 m rectangle having 2 free sides (opposite each other). The former case gives a frequency of 0.266 Hz, and the latter case gives a lower bound frequency of 0.233 Hz. Figure 4.2.2 shows a plot of the first mode of the sun-shield finite element model, which was found to occur at 0.23 Hz, which slightly underestimates the values predicted by the hand calculations. The slight underestimation is due to the coarseness of the mesh.

A sun-shield-only sub-model of the TPF system was analyzed to evaluate its effective mass characteristics. This model was constrained at the base of the deployable v-groove support booms. Figure 4.2.3 shows a plot of the modal frequency of the sun-shield assembly as a function of mode number. We can see a very high modal density for the sun-shield system: it has approximately 200 modes with frequencies less than 1 Hz, and almost 1000 modes with frequencies below 300 Hz.

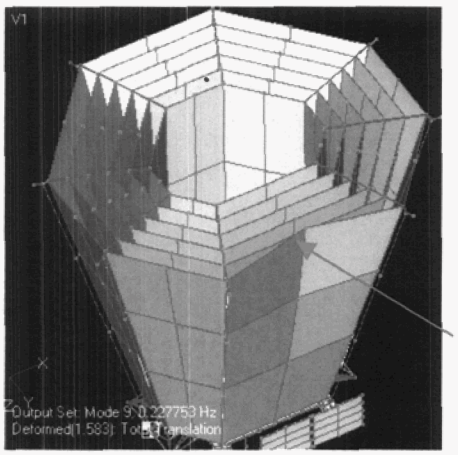


Fig. 4.2.2. First Mode of FEM V-groove Sun-shield

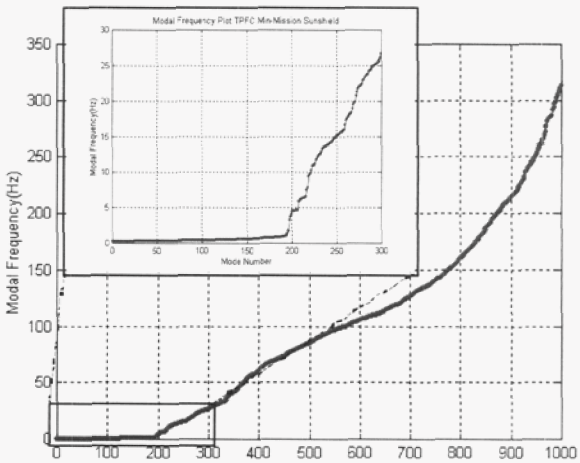


Fig. 4.2.3. Modal Frequencies for V-groove Sun-shield

4.2.4 is a plot of the cumulative effective modal mass. There is a rather large jump in the translational effective masses in the xy plane at modes198 and 199 (3.2 and 3.7 Hz). The mode shape for mode 198 is shown in. We can see that the mode shape is no longer a local one: there is significant participation of most of the structure. If one wants to capture 90% of the effective mass, then one would have to carry at least 500 modes to capture the translation terms, and at least 1000 modes to capture the rotational effective mass.

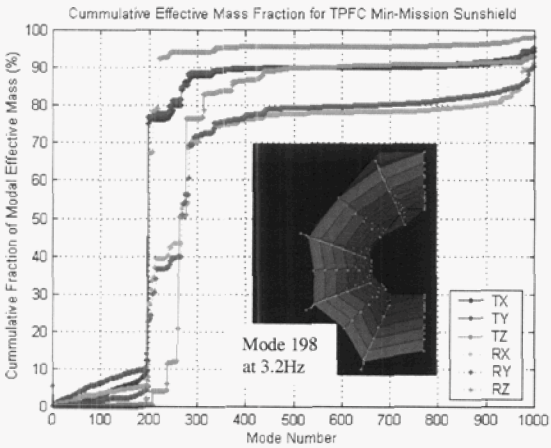


Figure 4.2.4. Cumulative Effective Modal Mass for Sun-shield

### 4.3. Reaction Wheel Jitter & Slew-Settle Analysis Results

Fig. 4.3.1 shows the computed line-of-sight (LOS) pointing response, as a function of reaction wheel operating speed, for the design having two stages of isolation. The LOS response is within requirement specifications for the expected range of operating speed for the reaction wheels. Figure 4.3.1 shows the rigid-body pointing transient response after a simulated 20 degree slew maneuver. The slew-settle time is manageable, even with our very flexible system.

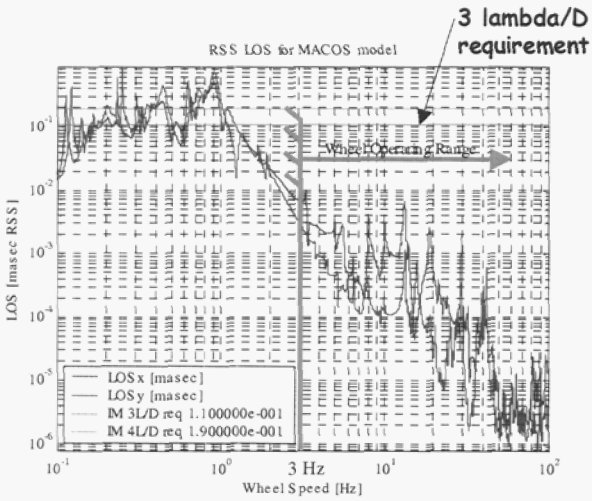


Fig. 4.3.1. LOS Pointing Error for Reaction Wheel Jitter

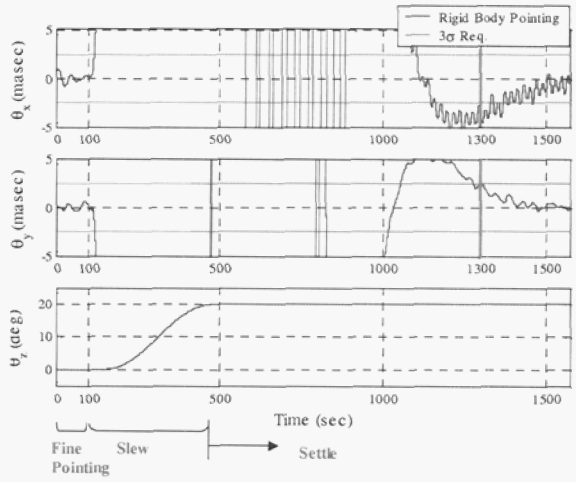


Fig. 4.3.2. Slew-Settle for Rigid-Body Pointing

## 5. CONCLUSION

The preliminary analyses conducted for thermal distortion and dynamic responses of the TPF-Coronagraph minimum mission design have shown system responses within the limits that could theoretically allow us to detect and characterize earth-sized planets orbiting near-by stars. Many more details of design and analysis need to be addressed in the design development process, but so far the potential looks promising. A comprehensive testing program will also be needed to demonstrate the feasibility of key technologies.

## REFERENCES


1. M. Levine, et al, *Terrestrial Planet Finder Coronagraph Minimum Mission Baseline Design and Analysis Report,* JPL 28535, April 22, 2004.
2. The Boeing Company, *Delta IV Payload Planner's Guide,* MDC 00H0043, October, 2000.
3. R.D. Blevins, *Formulas for Natural Frequency and Mode Shape*, Van Nostrand Reinhold Co. Inc., 1979, page 226.